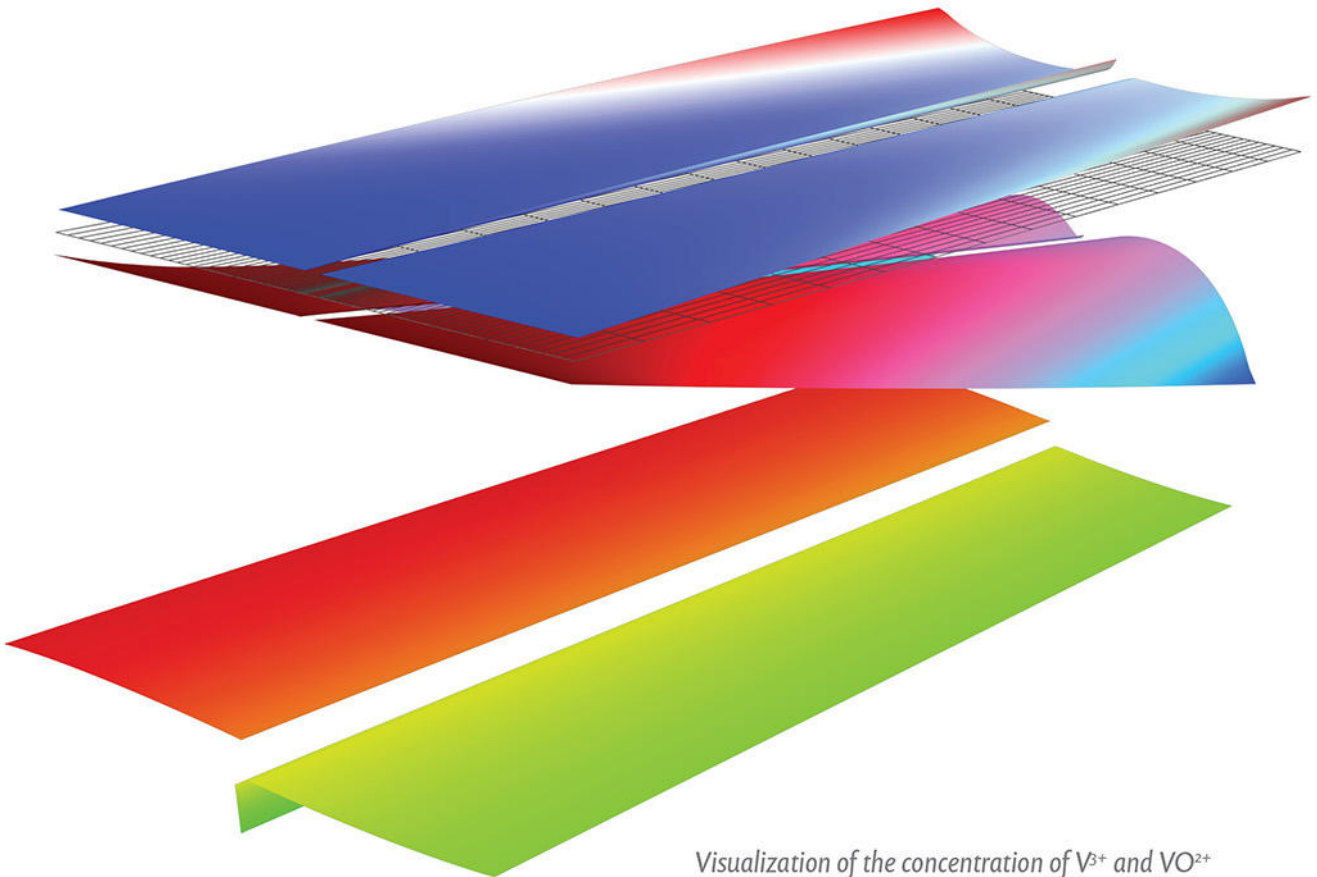# Scalable, durable, and safe enough for the power grid.

Visualization of the concentration of V^{3+} and VO^{2+} ions (top), V^{2+} and VO^{2+} ions (middle), and electrolyte potential (bottom) in a vanadium redox flow battery.

When developing rechargeable batteries for the power grid, vanadium is a stronger contender than lithium. Advantages include scalability, longer and more consistent operation lifetimes, safety, and the ability to fill in the gaps when wind or solar power suffers intermittency issues. But vanadium redox flow batteries (VRFBs) do bring shortcomings of their own. Engineers looking to improve grid energy storage and reliability often start by optimizing VRFB designs.

The COMSOL Multiphysics® software is used for simulating designs, devices, and processes in all fields of engineering, manufacturing, and scientific research. See how you can apply it to modeling vanadium redox flow batteries.

comsol.blog/VRFB

COMSOL

Vacuum-Assisted Growth of Low-Bandgap Thin Films (FA$_{0.8}$MA$_{0.2}$Sn$_{0.5}$Pb$_{0.5}$I$_3$) for All-Perovskite Tandem Solar Cells

Bahram Abdollahi Nejand,* Ihteaz M. Hossain, Marius Jakoby, Somayeh Moghadamzadeh, Tobias Abzieher, Saba Gharibzadeh, Jonas A. Schwenzer, Pariya Nazari, Fabian Schackmar, Dirk Hauschild, Lothar Weinhardt, Uli Lemmer, Bryce S. Richards, Ian A. Howard, and Ulrich W. Paetzold*

All-perovskite multijunction photovoltaics, combining a wide-bandgap (WBG) perovskite top solar cell ($E_G \approx 1.6$–1.8 eV) with a low-bandgap (LBG) perovskite bottom solar cell ($E_G < 1.3$ eV), promise power conversion efficiencies (PCEs) >33%. While the research on WBG perovskite solar cells has advanced rapidly over the past decade, LBG perovskite solar cells lack PCE as well as stability. In this work, vacuum-assisted growth control (VAGC) of solution-processed LBG perovskite thin films based on mixed Sn–Pb perovskite compositions is reported. The reported perovskite thin films processed by VAGC exhibit large columnar crystals. Compared to the well-established processing of LBG perovskites via antisolvent deposition, the VAGC approach results in a significantly enhanced charge-carrier lifetime. The improved optoelectronic characteristics enable high-performance LBG perovskite solar cells (1.27 eV) with PCEs up to 18.2% as well as very efficient four-terminal all-perovskite tandem solar cells with PCEs up to 23%. Moreover, VAGC leads to promising reproducibility and potential in the fabrication of larger active-area solar cells up to 1 cm^2.

In recent years, hybrid organic–inorganic perovskite materials attracted tremendous attention due to their outstanding optoelectronic and piezoelectric properties.[1–3] The optoelectronic properties of the perovskite materials enables power conversion efficiencies (PCEs) as high as 25.2% in single-junction perovskite thin-film solar cells.[4] Moreover, the wide range of bandgaps (E_G) of this class of materials generates enormous interest in perovskite-based multi-junction photovoltaics (PV).[1] To go beyond Shockley–Queisser radiative efficiency limit for single-junction solar cells, wide-bandgap (WBG) perovskite top solar cells ($E_G > 1.6$ eV)[5] are combined with high-efficiency low-bandgap (LBG) bottom solar cells made from Si,[6] CIGS[7] or LBG ($E_G < 1.3$ eV) perovskite devices.[8–10] While tandem PV technologies based on market-dominant crystalline Si and CIGS bottom solar cells have recently demonstrated PCEs exceeding 28%,[6,11] all-perovskite tandem solar cells are still less advanced. In comparison to single junction PSCs, all-perovskite tandem solar cells still lack behind with record PCEs of 23.1%[12] and 25%[12] for of all-perovskite two-terminal (2T) and four-terminal (4T) tandem solar cells, respectively.

The key challenges hindering the progress of all-perovskite tandem solar cells are the low performance and stability of the LBG perovskite bottom solar cells. To resolve these challenges, previous studies on LBG perovskite thin films addressed compositional engineering of the perovskite, strategies to improve the thin-film morphology, and routes to enhance the optical and electrical properties.[8,10,12–15] LBG

Dr. B. Abdollahi Nejand, I. M. Hossain, M. Jakoby,
S. Moghadamzadeh, S. Gharibzadeh, J. A. Schwenzer, P. Nazari,
F. Schackmar, Prof. U. Lemmer, Prof. B. S. Richards, Dr. I. A. Howard,
Dr. U. W. Paetzold
Institute of Microstructure Technology
Karlsruhe Institute of Technology
Hermann-von-Helmholtz-Platz 1
Eggenstein-Leopoldshafen 76344 Karlsruhe, Germany
E-mail: bahram.abdollahi@kit.edu; ulrich.paetzold@kit.edu

Dr. B. Abdollahi Nejand, I. M. Hossain, M. Jakoby, S. Moghadamzadeh,
Dr. T. Abzieher, S. Gharibzadeh, J. A. Schwenzer, F. Schackmar,
Prof. U. Lemmer, Prof. B. S. Richards, Dr. I. A. Howard, Dr. U. W. Paetzold
Light Technology Institute
Karlsruhe Institute of Technology
Engesserstrasse 13, 76131 Karlsruhe, Germany

Dr. D. Hauschild, Dr. L. Weinhardt
Institute for Photon Science and Synchrotron Radiation (IPS)
Karlsruhe Institute of Technology
Hermann-von-Helmholtz-Platz 1, Eggenstein-Leopoldshafen
76344 Karlsruhe, Germany

Dr. D. Hauschild, Dr. L. Weinhardt
Institute for Chemical Technology and Polymer Chemistry (ITCP)
Karlsruhe Institute of Technology
Engesserstr. 18/20, 76128 Karlsruhe, Germany

perovskite thin films are realized by careful compositional engineering, incorporating Sn at the site of Pb in multication perovskite crystal structures.[8,10,13] In this regard, the exact ratio of Sn to Pb is critical, since the incorporation of Pb in the Sn-based perovskite matrix increases the charge-carrier lifetime and decreases the E_G (to below the E_G of pure Sn-based perovskite materials) at the same time.[16,17] To date, the highest reported PCE for mixed Sn–Pb perovskites with pure iodine as a halogen—$MA_{0.5}FA_{0.5}Pb_{0.5}Sn_{0.5}I_3$—is 17.6%,[14,15] where MA and FA denote the organic cations of methylammonium and formamidinium, respectively. Moreover, by incorporating Cl^- and later guanidinium thiocyanate (GuaSCN), the PCE of the LBG PSC was increased to 20.4%.[9,12] It should be noted that these high PCEs are demonstrated exclusively for devices processed and characterized in an inert atmosphere. Sn-based perovskites are known to be highly sensitive to oxidation of Sn^{2+} to Sn^{4+}, which deteriorates the optoelectronic properties.[16,19] Several methods have been proposed in the literature to circumvent this oxidation in Sn-based perovskites, such as using protection additives like SnF_2,[18] $SnBr_2$,[18,20,21] $SnCl_2$,[20,21] and GuaSCN.[12] In fact, SnF_2 can suppress the oxidation of the Sn compounds, leading to more stable thin films.[22,23]

Next to the composition of the LBG perovskite thin films, film formation and morphology are key to performance and stability. Most LBG PSCs are processed using the antisolvent method, whereby antisolvents promptly remove the precursor solvents—dimethylformamide (DMF) and dimethyl sulfoxide (DMSO)—from the wet film and initiate fast nucleation and crystal growth of the multicrystalline perovskite thin film. However, the antisolvent method is also known to produce rather small LBG perovskite grains in the range of only a few-hundred nanometers.[24–27] While it was shown that these small grains (accompanied by a large number of grain boundaries in the film) do not cause severe problems in Pb-based perovskite thin films, they are reported to be detrimental in Sn-based perovskite thin films[24–27] due to lots of defects at the grain-boundaries. Therefore, controlling the nucleation and crystal growth in Sn-based LBG perovskites is essential for achieving thin films of high optoelectronic quality. To further improve the morphology and crystal quality of LBG perovskite thin films, several studies investigated the ratio of halogens in the LBG perovskite thin films.[19,28] It was reported that in the LBG PSCs, similar to perovskites with regular-bandgap ($E_G \approx 1.5$–1.6 eV), the addition of chloride anions increases the average grain size and reduces electronic disorder in the mixed perovskite absorber thin films.[19,29] Furthermore, the incorporation of Br^- in the mixed Sn–Pb LBG perovskite can strongly reduce charge-carrier density and increase the Urbach energy. However, it was presented that incorporating small amounts of Br^- (0.06 wt%) effectively passivates the grain boundaries.[28] In perovskite thin films, grain boundaries are known as being potential sites for nonradiative recombination of charge carriers.[28] Several attempts were conducted to reduce the grain boundaries in LBG perovskites using two-step methods,[30] MACl vapor treatment,[19] and hot-casting methods.[13] Among these methods, hot-casting resulted in microcrystalline perovskite grains but the electrical quality of the crystallites was very poor, exhibiting a low charge-carrier lifetime of 0.95 ns.[13] Thus, a fabrication method that allows processing large grains with high electrical quality would induce an outstanding development for LBG PSCs.

In this work, vacuum-assisted growth control (VAGC) is introduced to control the thin-film formation of LBG mixed-cation perovskites in the composition of $FA_{0.8}MA_{0.2}Sn_{0.5}Pb_{0.5}I_3$. As it is shown throughout the paper, VAGC allows the modification of the LBG perovskite microstructure to realize pinhole-free perovskite thin films of large grains with improved charge-carrier lifetimes as well as optoelectronic properties compared to LBG perovskite thin films processed by the conventional antisolvent method. In particular, employing the VAGC to fabricate LBG PSCs ($E_G \approx 1.27$ eV), a high PCE of 18.2% is demonstrated which is among one of the highest reported pure iodine-based LBG PSCs (with no additives such as Br^-,[28] Cl^-,[31] and GuaSCN[12]). Finally, using the current LBG PSC processed by VAGC in combination with a semitransparent regular-bandgap ($E_G \approx 1.63$ eV) PSCs in a 4T all-perovskite tandem solar cell, an efficient PCE of 23% and a stabilized PCE (SPCE) of 21.8% are achieved.

To date, the deposition of LBG perovskite thin films is conducted by spin-coating the precursor solution and extracting the solvents in an antisolvent step using toluene,[14] chlorobenzene,[30] diethyl ether,[22] or anisole[19] followed by an annealing step. The choice of the antisolvent allows controlling the morphology of the perovskite thin film, which, in turn, determines the optoelectronic properties and PV characteristics of the LBG PSCs.[32] For the established triple-cation PSCs, the antisolvent method yield thin films with dense and compact grains in the range of a few-hundred nanometers.[24–27] In this work, VAGC is employed as an alternative strategy to initiate nucleation in the solution-processed perovskite wet films, making use of an abrupt vacuum step to promptly evaporate the solvents (see **Figure 1**a,b). As shown in Figure 1a,b, the perovskite thin film produces in the vacuum chamber by ejecting the solvents (DMF and DMSO) followed by annealing on the hotplate. Perovskite thin films prepared by this method exhibit large columnar grains with almost no grain boundaries perpendicular to the thin-film surface (see Figure 1c). The columnar grain orientation in the LBG perovskite thin films is expected to be beneficial, as it allows fast transportation of charge carriers across the perovskite thin film to the selective contacts at the perovskite/electron transport layer (ETL) and perovskite/hole transport layer (HTL) interfaces. Making use of the large columnar LBG perovskite grains produced by VAGC in this work, PSCs with PCE as high as 18.2% are demonstrated, exceeding the 15.4% of reference devices prepared by the established antisolvent method (Figure 1d). Moreover, these devices also demonstrate good long-term stability in the stabilized PCE (SPCE) up to 17.1% under constant air-mass 1.5 global (AM 1.5G) solar illumination and 300 s of maximum power-point (MPP) tracking, illustrated in Figure 1e. The long-term MPP tracking of the prepared devices by VAGC and the antisolvent method shows similar photo-stability for PSC prepared by VAGC compared to the antisolvent method (Figure S1, Supporting Information) for devices stored at 25 °C in N_2 atmosphere. It should be noted that, to date, this represents one of the highest PCEs of the LBG PSC based on pure iodine halogen without incorporation of Br^-,[28] Cl^-[31] nor incorporation of additives such as GuaSCN.[12] The SEM image inset in Figure 1e demonstrates the surface morphology of the large-grain LBG perovskite thin film produced by VAGC with a 10 s vacuum step. The optimization of
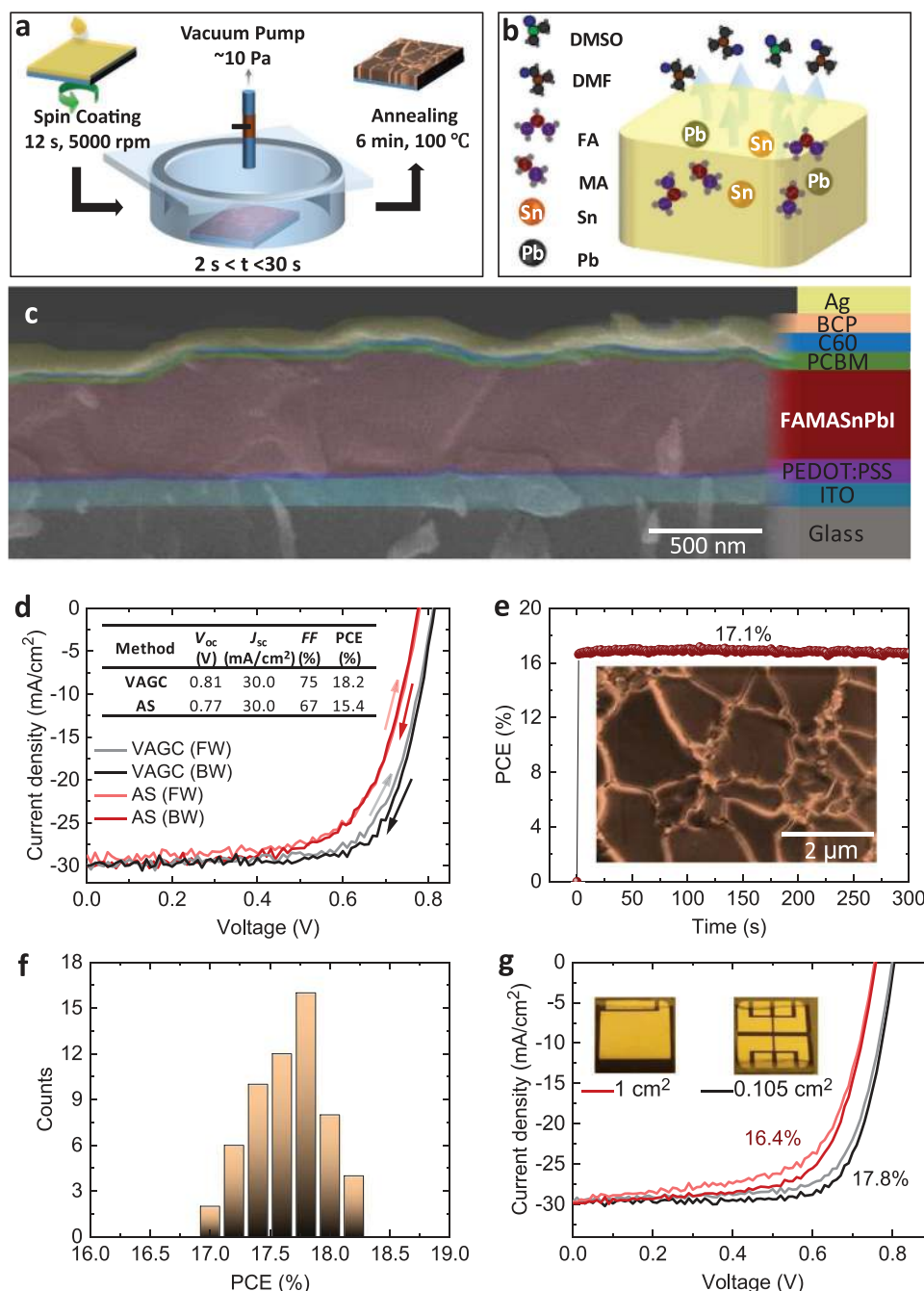
ADVANCED
SCIENCE NEWS

www.advancedsciencenews.com

ADVANCED
ENERGY
MATERIALS

www.advenergymat.de

Figure 1. a,b) Schematic illustration of the vacuum-assisted growth control method for processing high-quality low-bandgap (LBG) perovskite thin films. c) Cross-section scanning electron microscopy (SEM) image of the LBG PSC. d) Comparison of the current density–voltage (J–V) characteristics of the best performing solar cells prepared via the VAGC and antisolvent (AS) method, respectively, reveal significant enhancement in open-circuit voltage (V_{OC}) and fill factor (FF) for devices prepared via the VAGC. e) Stabilized power conversion efficiency (SPCE) of the best performing solar cell under maximum-power-point tracking conditions. In the inset, a top surface SEM image of the LBG perovskite thin film with micrometer-sized grains is provided. f) Device histogram for 58 samples, and g) J–V characteristics of champion devices with active areas of 0.105 and 1 cm².

the vacuum time will be discussed later. The thin-film architecture of the reported LBG PSC is glass/indium tin oxide (ITO)/poly(3,4ethylenedioxythiophene):polystyrene sulfonate (PEDOT:PSS)/($FA_{0.8}MA_{0.2}Sn_{0.5}Pb_{0.5}I_3$)/phenyl-$C_{61}$-butyric acid methyl ester (PCBM)/fullerene (C_{60})/2,9-dimethyl-4,7-diphenyl-1,10-phenanthroline (BCP)/Ag, as illustrated in Figure 1c. The

perovskite is processed with a Pb to Sn molar ratio of 1:1. The molar ratio of the organic cations FA to MA is optimized to 4:1 with regard to stable LBG PSC. For more details on the device fabrication, the reader is directed to the methods section.

By adopting the mass flow rate and vacuum time during the VAGC, the solvent extraction is manipulated, allowing to

ADVANCED
SCIENCE NEWS
www.advancedsciencenews.com

ADVANCED
ENERGY
MATERIALS
www.advenergymat.de

control the grain size of the microcrystalline perovskite thin films.[33] A vacuum pressure base of 10 Pa is maintained during VAGC which implies prompt extraction of the solvents given the vapor pressure of DMF (≈360 Pa)[34] and DMSO (≈56 Pa).[34] However, it should be noted that in the perovskite solutions, DMF and DMSO are known to form chemical complexes with PbI_2 and SnI_2.[25] Complexed DMSO and DMF are much more challenging to be removed during the vacuum step and likely will only exit from the film during the subsequent annealing[25] at around 100 °C. The champion device reported in Figure 1d used VAGC for 10 s of vacuum time. This optimum vacuum time is determined among four vacuum times presented in Figure S2a (Supporting Information). Similarly to the reference devices prepared by the antisolvent method, the solar cells prepared with short vacuum times (<10 s) suffer from a lower open-circuit voltage (V_{OC}), fill factor (FF), and current density (J_{SC}) (Figure S2b–d, Supporting Information). On the other hand, as shown in Figure S2a (Supporting Information), longer vacuum times (30 s) deteriorate the PCE of the LBG PSCs as well, which will be investigated in more detail as part of the photophysical characterization later in this work. As shown in Figure S2e (Supporting Information), the enhancement in J_{SC} with vacuum time is confirmed by external quantum efficiencies (EQE) measurements. Given that the absorptance of the perovskite layers prepared for various vacuum times remains similar (Figure S2f, Supporting Information), it can be concluded that the internal quantum efficiency in the perovskite solar cells increases with vacuum time. This enhancement in internal quantum efficiency can be attributed to reduced nonradiative recombination losses in the perovskite layer, leading primarily to a strong enhancement in V_{OC} (Figure S2c, Supporting Information) possible along with an improved charge carrier collection efficiency. Besides the improved quality of the perovskite absorber layer (Figure S2g, Supporting Information), also a stronger quenching of the photoluminescence (PL) signal for perovskite layers prepared with longer vacuum times is observed if covered with the PCBM/C60 as an ETL (see Figure S2h, Supporting Information). The enhanced quenching indicates that charge carrier transport is facilitated at the perovskite/ETL (PCBM/C60) interface for perovskite layers prepared with long vacuum times. For the antisolvent method, crystallization of the perovskite thin film is initiated at the point when the antisolvent is dripped onto the wet film of the spin-coated precursor solution. Given the short timeframes and a large number of poorly controlled experimental variables (including dripping the antisolvent, the purity of the antisolvent, the dripping duration, angle of the pipette), LBG perovskite thin films produced by the antisolvent method are difficult to control at whole parts of the surface. Therefore, in general, the antisolvent method is prone to numerous uncertainties in the reproducibility of the prepared devices, while LBG perovskite solar cells processed by VAGC demonstrate a high PCE and reproducible performance (see Figure 1f). The homogeneous removal of the solvents over the entire area is assumed to be one of the keys to achieve a good reproducibility (Figure 1f; Figure S2a, Supporting Information). Next to the improved reproducibility of devices processed by VAGC (here 58 samples), this method is an appropriate candidate for upscaling of the LBG PSCs. To demonstrate this, an LBG PSC with 1 cm² active area is fabricated and the performance is compared to that of a PSC with a small active area of 0.105 cm² in the same batch (see Figure 1g). As shown, a slightly reduced PCE of 16.4% is observed for PSC with 1 cm² aperture area compared to the best small-area PSC, which exhibits 17.8% PCE.

Having demonstrated that VAGC is a promising route to process high-quality LBG perovskite thin films and high-efficiency solar cells, the morphology of these thin films are studied in detail with respect to the vacuum time during VAGC. Scanning electron microscopy (SEM) images of the surface of the LBG perovskite thin films prepared by VAGC and a subsequent annealing step on a hotplate (100 °C, 5 min) show that increasing the vacuum time (2, 5, 10, and 30 s) leads to larger grains in the perovskite thin film (**Figure 2**a–d). As illustrated in Figure 2a, by exposing the wet thin film to vacuum for just 2 s and subsequent annealing on a hotplate, the film exhibits only small grains of <400 nm in diameter. As shown in Figure 2a–c, with increasing vacuum time to 10 s, the primary LBG perovskite grains increase in size and the surface area covered with small grains decreases. By further increasing the vacuum time, the size of the grains slightly decreases (Figure 2d). For 10 s vacuum time, the primary grains exceed diameters of 2 µm and the small grains almost vanish completely (Figure 2c). Furthermore, the undesired pinholes, which are observed at lower vacuum time <10 s, disappear with increasing vacuum time (Figure 2a–c). Perovskite thin films with large grain and pinhole-free morphology have been reported to be promising for solar cells[29,35] and also in our study, these perovskite thin films yield devices with high PCEs (Figure 1; Figure S2a, Supporting Information). The observed increase in primary perovskite grain size with increasing vacuum time is attributed to the vacuum-induced nucleation and perovskite nuclei growth by prompt removal of the solvents from the wet film. For too short vacuum times <5 s, the growth of the perovskite grains is expected to be incomplete and larger amounts of small grains appear at the surface of the thin film. For longer vacuum times ≥10 s, the growth of the perovskite grains saturates as the perovskite thin film consists of densely packed grains with diameters >2 µm. In Figure S3 (Supporting Information), a schematic illustration is provided to propose the suggested morphology formation of the LBG perovskite thin film during VAGC of different vacuum times followed by the annealing step.

It is important to note that the LBG perovskite thin films fabricated by VAGC show significantly larger perovskite grains compared to those reference perovskite thin film processed by the antisolvent method (see Figure 2e). Moreover, the LBG thin films processed by the antisolvent method reveal horizontal grain-boundaries normal to the direction of the charge-carrier transport in the film (see Figure 2f), while the perovskite thin films processed by VAGC show large columnar grains almost without grain boundaries normal to the charge transport (see Figure 2g). More SEM images from cross-section of the prepared devices by VAGC and antisolvent and the grain size statistic is shown in Figure S4 (Supporting Information) and Figure 2h, respectively. Both aspects are key to explain that the VAGC enables high-quality LBG perovskite thin films since grain boundaries are a source of recombination centers reducing the lifetime and, in turn, the diffusion length of
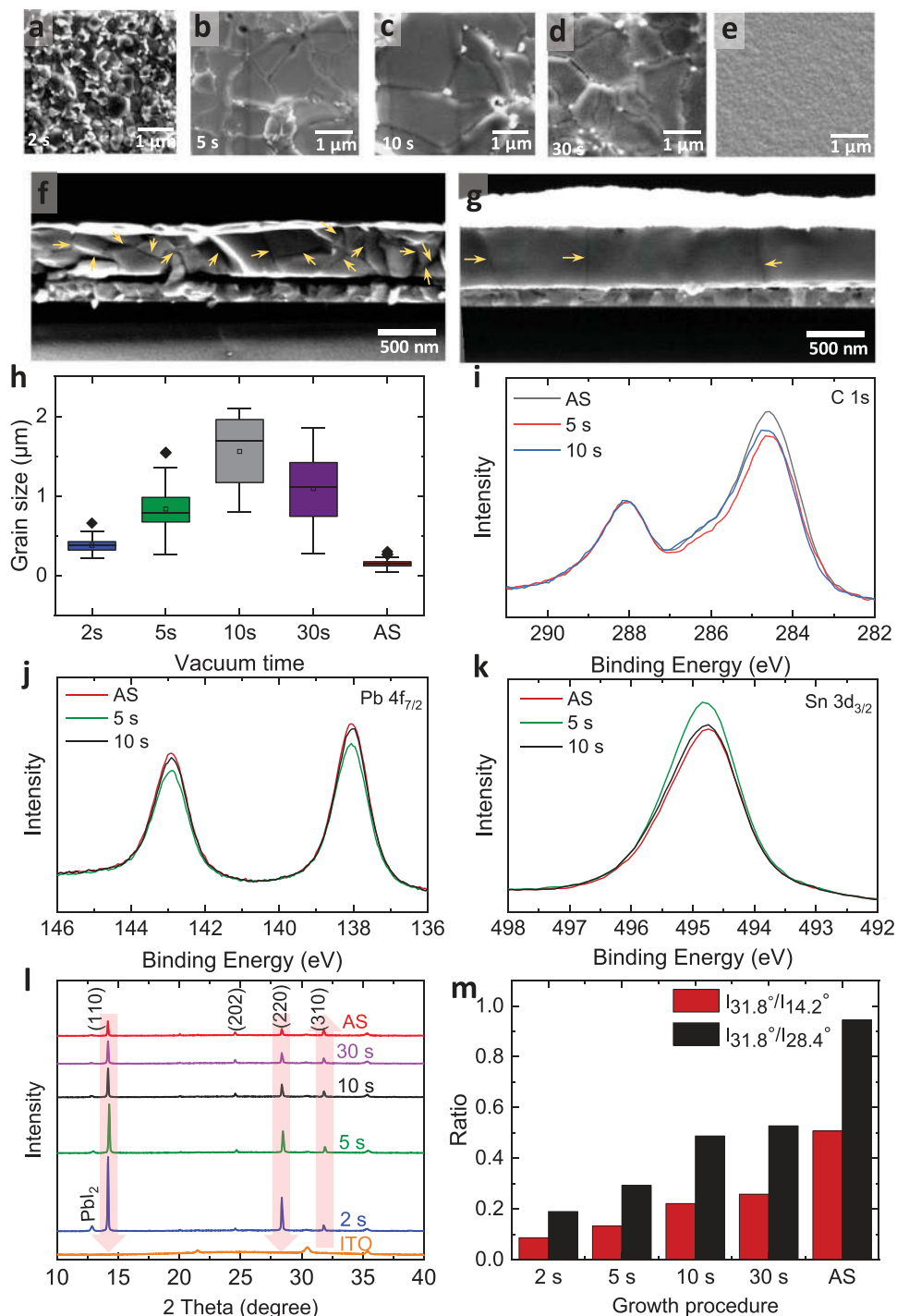
ADVANCED
SCIENCE NEWS
www.advancedsciencenews.com

ADVANCED
ENERGY
MATERIALS
www.advenergymat.de

Figure 2. SEM images of the deposited perovskite thin films by VAGC for different vacuum exposure times: a) 2 s, b) 5 s, c) 10 s, and d) 30 s. e) SEM image of a LBG perovskite thin film prepared by antisolvent (AS) method. f) The corresponding cross-section images of the perovskite thin films grown by the antisolvent method and g) VAGC. h) Grain size statistics of the produced perovskite films at different vacuum times of VAGC and antisolvent method. XPS spectra of i) the C 1s, j) the Pb $4f_{7/2}$, and k) the Sn $3d_{3/2}$ region of the samples prepared by the antisolvent method, the 5 s, and 10 s VAGC. The XPS survey spectra are shown in Figure S5 in the Supporting Information. l) X-ray diffraction patterns and m) peak intensity ratios for deposited perovskite thin films grown by VAGC (vacuum times of 2–30 s) and antisolvent method.

charge carriers. This decrease of horizontal grain boundaries in the perovskite thin films is in good agreement with the observed increase in PCE and V_{OC} of the devices processed

by VAGC compared to the antisolvent method (Figure 1d). As shown in Figure 2a–d, there are some white regions on the surface of the perovskite layers, which are disappearing by increase

the vacuum time. To study this white region, surface-sensitive X-ray photoelectron spectroscopy (XPS) measurements of the LBG perovskite thin films processed by the antisolvent method, the 5 s, and the 10 s VAGC are conducted. The XPS survey spectra (see Figure S5 in the Supporting Information) show all expected photoemissions and Auger peaks, e.g., C 1s, N 1s, Sn 3d, Pb 4f, and I 3d. At first glance, the three survey spectra appear similar. Despite some small variations, the most obvious difference is an increase of the Sn-related intensities for the 5 s VAGC samples. To analyze the variations, the C 1s, Pb $4f_{7/2}$, and Sn $3d_{3/2}$ detail spectra are shown in Figure 2i–k. The C 1s spectra exhibit two main peaks at ≈288.0 and ≈284.6 eV and a shoulder at ≈286 eV. These features are indicative for the organic cations of FA and MA.[5,36] The sample prepared by the antisolvent method shows highest value of the organic cations on the surface while the prepared sample at vacuum time of 5 s shows the lowest C-related intensity (Figure 2i). A qualitative analysis of the Pb $4f_{7/2}$ signals show that the 5 s VAGC sample exhibits the lowest Pb intensity, followed by the 10 s, and the antisolvent sample (Figure 2j). In contrast, the Sn 3d signal is strongest for the 5 s vacuum time, decreases in intensity for the 10 s VAGC sample and is lowest for the antisolvent sample (Figure 2k). In addition, the main peak at ≈494.8 eV can be related to Sn^{2+}. Accordingly, the 5 s sample shows the highest amount of Sn^{2+}, which decreases (relative and absolute) for the 10 s sample. This result is aligned with the decrease of the white regions in the SEM images (Figure 2a–d), which is a strong indication that these white regions consist of a Sn-rich phase, possibly SnI_2. This suggests that a growth time of 5 s in vacuum for the perovskite is not long enough to form the right stoichiometric composition. Furthermore, these white regions in the interface of the perovskite and ETL can be original of hindering the charge extraction, which is observed in Figure S2h (Supporting Information), and consequently lower current density at lower vacuum time (Figure S2d, Supporting Information).

In order to trace the structural transformation of the LBG perovskite thin films processed by VAGCs for different vacuum times, X-ray diffraction of these thin films are compared to LBG perovskite thin films processed by the antisolvent method (see Figure 2l,m). As a reference, pure Sn- and Pb-based perovskite thin films with compositions $FA_{0.8}MA_{0.2}SnI_3$ and $FA_{0.8}MA_{0.2}PbI_3$ are compared (see Figure S6a,b in the Supporting Information). By increasing the vacuum time, the intensities of the characteristic peaks of the perovskite structure at 14.2° and 28.4° decrease, while the intensity of the characteristic perovskite peak at 31.8° slightly increases (see Figure 2l,m). This gradual change in relative height of the perovskite peaks in the XRD pattern is a very strong indication of a gradual change in crystal orientation in the perovskite thin films along with increasing vacuum time. Moreover, compared to the reference mixed Sn–Pb LBG perovskite thin film processed by the antisolvent method, the higher peak intensity in the XRD pattern (see Figure S6a,b in the Supporting Information) suggests a higher crystallinity for the LBG perovskite thin films processed by VAGC. Interestingly, the fast crystallization of the pure Sn-based perovskite structure produces perovskite crystals with very low intensity compared to the pure Pb-based perovskite and much less than the

mixed Sn–Pb perovskite (Figure S6a, Supporting Information). Moreover, as shown in Figure S6a (Supporting Information), a strong hexagonal nonperovskite phase (δ-phase) peak[37] is observed in the $FA_{0.8}MA_{0.2}PbI_3$ (located at 12°), which does not appear in the XRD pattern of $FA_{0.8}MA_{0.2}Sn_{0.5}Pb_{0.5}I_3$ prepared by the antisolvent method and VAGC (Figure S6a, Supporting Information). Furthermore, in the experiment, it was visually observed that the formation time needed to form the perovskite thin films in the vacuum chamber follows the order $FA_{0.8}MA_{0.2}PbI_3$ < $FA_{0.8}MA_{0.2}Sn_{0.5}Pb_{0.5}I_3$ < $FA_{0.8}MA_{0.2}SnI_3$ (see supporting videos and more details in Supporting Information). Furthermore, according to the full width at halfmaximum (FWHM) extraction, the crystal size of the mixed Pb-Sn perovskite is between the pure Pb-based and pure Sn-based perovskite structures (Figure S3a,b, Supporting Information). Therefore, the XRD results and visual observation indicate that the mixture of Sn and Pb significantly alters the perovskite crystal growth by fast nucleation of the Sn-rich perovskite to control the crystal growth direction followed by a contribution of the Pb component in the $FA_{0.8}MA_{0.2}Sn_{0.5}Pb_{0.5}I_3$ crystal structure. To further investigate the surface of the perovskite thin films grown by VAGC and the antisolvent method, Kelvinprobe force microscopy (KPFM) analysis is conducted in the dark and in ambient atmosphere (Figure S7, Supporting Information). It should be noted that KPFM measurements conducted in an ambient atmosphere can be affected by moisture or oxygen. However, the presented data still support the hypothesis that the perovskite thin films prepared by VAGC and the antisolvent method differ strongly and show a different material quality by contact potential difference (CPD) variation at the surface for both thin films. The detailed information is provided in the Supporting Information.

To study the charge-carrier lifetime in the perovskite thin films by time resolved photoluminescence (TRPL), two architectures are selected as follows: a) LBG perovskite thin films on insulating bare glass substrates and b) LBG perovskite thin films deposited on PEDOT:PSS as an HTL on a glass/ITO substrates (**Figure 3**a,b). Poly(methyl methacrylate) PMMA is used as an encapsulating layer on the perovskite layer in both architectures. The perovskite thin film deposited on the bare glass substrate reveals the monomolecular lifetime of the charge carriers in the film limited only by nonradiative recombination at grain boundaries and bulk defects. As shown in Figure 3a, the LBG perovskite thin films processed by VAGC with 2 s vacuum time exhibit a low carrier lifetime of around 86 ns. With increasing vacuum time, the charge-carrier lifetime increases to 89, 220, and 105 ns, for vacuum times of 5, 10, and 30 s, respectively (Figure 3a; Table S1, Supporting Information). The longest charge-carrier lifetime of 220 s is demonstrated for the LBG perovskite thin films processed with 10 s vacuum time, which underlines the high quality of this LBG perovskite absorber thin film. These process parameters are also used for the champion device presented in Figure 1d. The increase in lifetime corresponds to a decrease in nonradiative recombination, which correlates again with the increase of the number of large grains for the perovskite thin films processed with longer vacuum times (see Figure 2). Moreover, as shown in Figure 3a and Table S1 (Supporting Information), we also
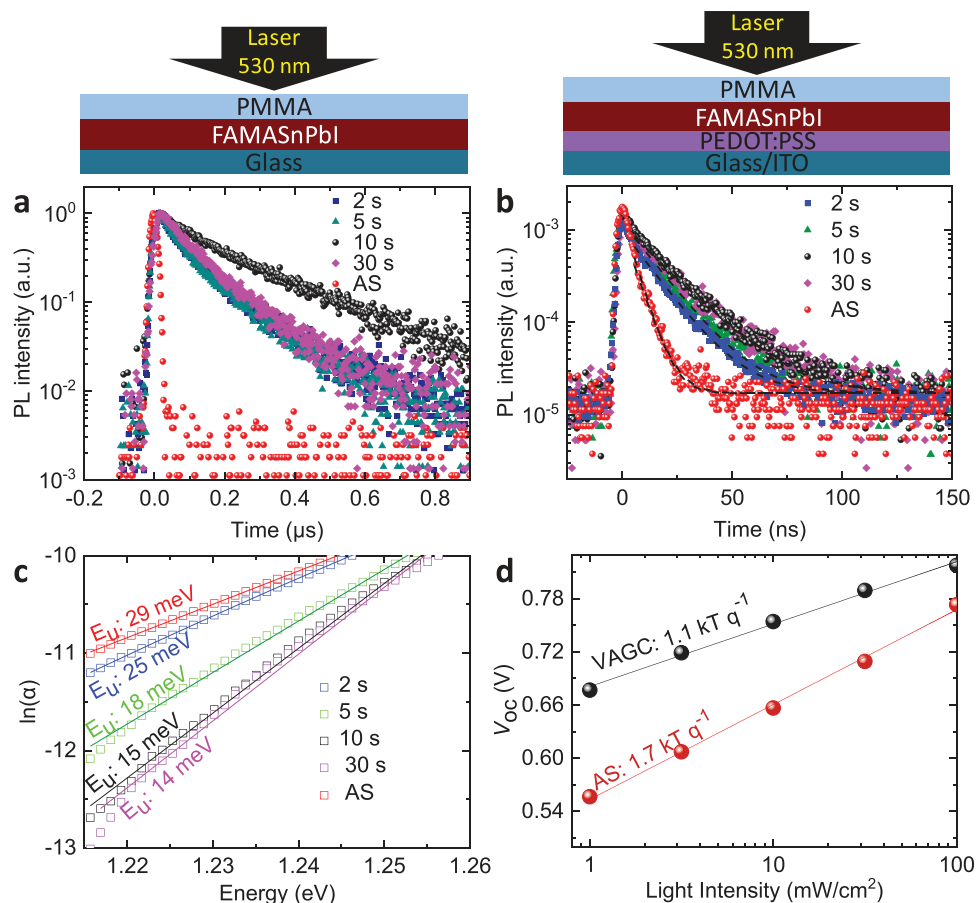
Figure 3. Time-resolved PL (TRPL) measurements of LBG perovskite thin films on a) bare glass and b) PEDOT:PSS/ITO substrates encapsulated with 150 nm PMMA. c) $\ln(\alpha)$ versus energy plotted to extract the Urbach energy (E_u) of perovskite thin films prepared by the VAGC and antisolvent (AS) method, and d) ideality factor measurement of LBG PSCs prepared by VAGC and antisolvent method.

find that the charge-carrier lifetime of the LBG perovskite thin films processed by the antisolvent method are >20 times lower than for VAGC (10 ns vs 220 ns). This difference is attributed to the improved morphology, namely the larger grains with less horizontal grain boundaries in the LBG perovskite thin films prepared by VAGC compared to those prepared by the antisolvent method (Figure 2f,g). This finding is in agreement with the higher V_{OC} and FF for LBG PSCs prepared by VAGC compared to the antisolvent method (Figure 1d). In the presence of PEDOT:PSS as underlying HTL on the glass/ITO, the charge-carrier lifetime of the deposited LBG perovskite thin film with VAGC is in the order of 13–18 ns while the LBG perovskite thin film prepared by the antisolvent method presents a charge-carrier lifetime of 5 ns (Figure 3b; Table S1, Supporting Information). This indicates that in the both VAGC and antisolvent method, the smaller grains cause faster extraction of charge carriers at the perovskite/HTL interface resulting in photoluminescence (PL) quenching.

The quality of the band edge of the LBG perovskite thin films prepared by VAGC and antisolvent method are compared by evaluating the Urbach energy. The energy disorder at the band edge, which is quantified by the Urbach energy (E_u), can be estimated using the expression

$$\ln(\alpha) = \ln(\alpha_0) + E/E_u \qquad (1)$$

where α is the absorption coefficient, E_u is the Urbach energy, and $E(=h\upsilon)$ is the photon energy.[38] As illustrated in Figure 3c, increasing the vacuum time results in a decrease of the E_u of the prepared LBG perovskite thin films from 25 to 14 meV, representing a very noticeable decrease in disorder. In other words, this increase in the vacuum time abates density of traps states close to the band edge of the LBG perovskite thin films. This result is in good agreement with TRPL results (Figure 3a) as well as PV characteristics (Figure S2a–d, Supporting Information). It suggests that the VAGC-processed perovskite thin films exhibit improved quality. Moreover, compared to the LBG perovskite thin films processed by the antisolvent method (E_u = 29 meV), the films processed by VAGC with vacuum times >5 s show less disorder, indicating lower trap densities close to the bandgap. Decreasing the trap density by longer vacuum-exposure times diminishes the possible trap-assisted recombination, which leads to considerable enhancement in the device performance (Figure 1d; Figure S2a–d, Supporting Information). In addition to the TRPL, the improved quality of the LBG perovskite thin films employed in the solar cells is verified by comparing the dark saturation current densities and the ideality factor in devices prepared by VAGC and antisolvent

ADVANCED
SCIENCE NEWS
www.advancedsciencenews.com

ADVANCED
ENERGY
MATERIALS
www.advenergymat.de

method. The lower dark saturation current density of the PSCs with LBG perovskite absorber thin films prepared by VAGC highlights that these devices suffer less from nonradiative recombination (see Figure S8 in the Supporting Information). Finally, the ideality factor determined by light-intensity-dependent V_{OC} measurements of the champion PSCs prepared by VAGC and the reference devices prepared by the antisolvent method are presented in Figure 3d. The ideality factor is significantly reduced for the LBG PSC prepared by VAGC to $n \approx 1.1$ in the vacuum time of 10 s. This is a further indication that the nonradiative bulk recombination (Shockley–Read–Hall type, with $n = 2$) is decreased and the relative amount of the intrinsic radiative recombination ($n = 1$) is enhanced (Figure 3d). In contrast, the solar cell prepared by the antisolvent method shows $n \approx 1.7$ indicating comparably stronger SRH recombination (Figure 3d). Overall, we demonstrate different surface and bulk sensitive characterization methods encompassing material characterization (PL, TRPL, Urbach energy, XPS) as well as device characterization (ideality factor, dark saturation current) that the LBG PSCs prepared by VAGC employ perovskite thin films with less nonradiative recombination losses compared to those prepared by the antisolvent method.

Finally, the high-performance LBG perovskite thin-film solar cells developed as part of this contribution are employed in all-perovskite 4T thin-film solar cells. The 4T perovskite-perovskite tandem solar cells are stacked using a bottom LBG PSC ($E_G \approx 1.27$ eV; see absorptance and Tauc plot in Figure S9a–c in the Supporting Information) prepared by VAGC and a conventional semitransparent regular-bandgap ($E_G \approx 1.63$ eV; see absorptance and Tauc-plot in Figure S9d in the Supporting Information) perovskite top solar cell (see **Figure 4**a). Figure 4b demonstrates the *J–V* characteristic of the 4T all-PSC. The top semitransparent solar cell has a regular configuration of ITO/SnO$_2$/Cs$_{0.1}$(MA$_{0.17}$FA$_{0.83}$)$_{0.9}$Pb(I$_{0.83}$Br$_{0.17}$)$_3$/2,2′,7,7′-tetrakis[N,N-di-(4-methoxyphenyl)amino]-9,9′-spirobifluorene (spiro-MeOTAD)/MoO$_x$/ITO/MgF$_2$. The MoO$_x$ thin film (10 nm) is used to protect the spiro-MeOTAD against ion bombardment during the subsequent ITO sputtering process and hole buffer thin film.[39,40] A conventional MgF$_2$ thin film (200 nm) on the sputtered ITO is used as an antireflection coating to increase the optical transmittance.[41] As shown in Figure 4b,c, the corresponding 4T all-PSC shows a remarkable PCE of 23.0% and SPCE of 21.8% (Figure 4b,c). The PCE of the all-perovskite 4T solar cell is determined by summing the PCE of the semitransparent regular-bandgap ($E_G \approx 1.63$ eV) PSC and filtered LBG PSC (Figure 4a). The champion LBG PSC processed by VAGC shows an outstanding PCE of 18.2% (SPCE of 17.1%) under AM 1.5G solar illumination and 4.5% SPCE by using the semitransparent regular-bandgap PSC as a light filter. By filtering the light with the semitransparent regular-bandgap PSC, the current density of the LBG PSC decreases from 30 to 8.5 mA cm^{-2} (see Figure 4b). The semitransparent regular-bandgap perovskite solar cell with normal architecture provides 18.5% (and SPCE of 17.3%) PCE (Figure 4b,c). Furthermore, the reflectance and transmittance of the regular bandgap as well as EQE of the semitransparent regular bandgap top solar cell and LBG bottom solar cell with and without the semitransparent regular bandgap top solar cell as a filter are shown in Figure S9e,f (Supporting Information).
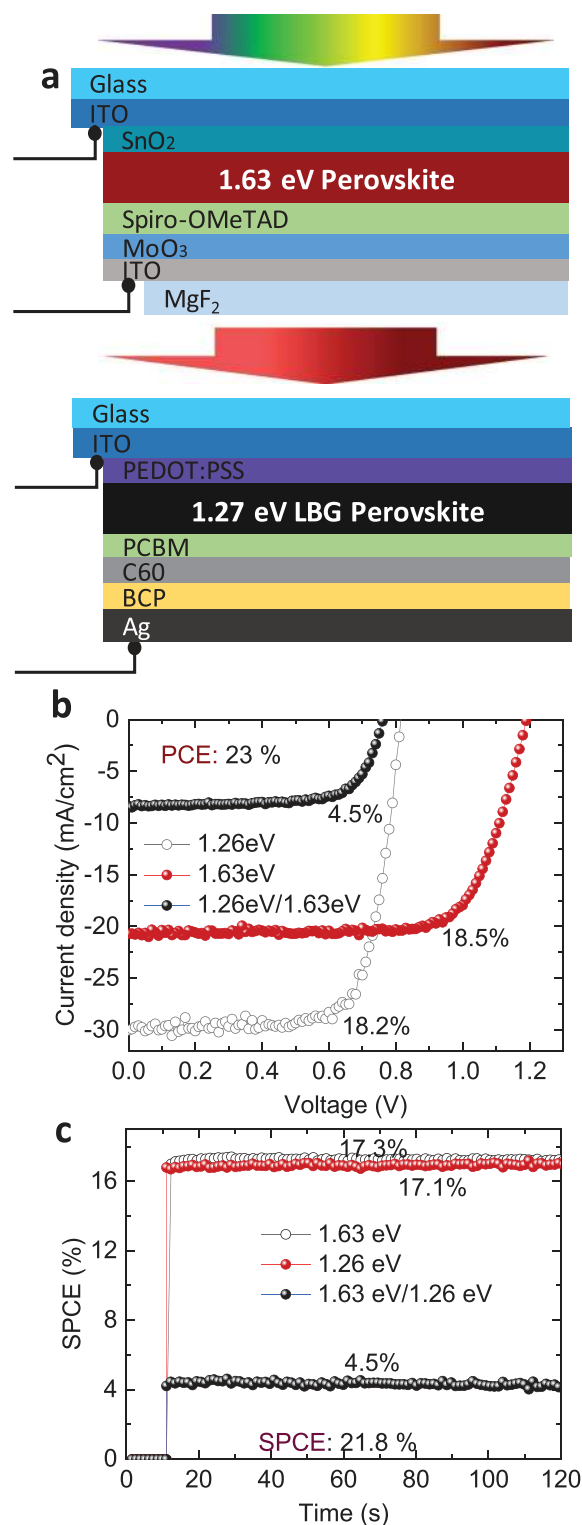

Figure 4. a) Schematic cross-section of the 4T all-perovskite tandem architecture. b) *J–V* characteristics of the single junction LBG bottom solar cell ($E_G = 1.27$ eV), the single junction semitransparent regular-bandgap top solar cell ($E_G \approx 1.63$ eV), and the filtered LBG bottom cell under AM 1.5G illumination measured in backward direction. c) Stabilized power conversion efficiency of the corresponding solar cells measured >100 s at MPP tracking of the champion 4T all-perovskite tandem solar cell, namely, the LBG bottom solar cell and the semitransparent perovskite top solar cell.

These results demonstrate the potential of VAGC in the reproducible fabrication of high efficiency LBG perovskite solar cells as well as an efficient 4T all-perovskite tandem solar cell.

In summary, in this work, high-quality LBG perovskite thin films are prepared by VAGC. These films demonstrate large columnar grains compared to the reference devices prepared by the conventional antisolvent method. The improved film quality of the LBG perovskite thin films prepared by VAGC results in a strongly enhanced charge-carrier lifetime, namely 22 times longer than for the conventional antisolvent method. For an optimal vacuum annealing time, the resulting low-bandgap perovskite solar cells show a remarkable PCE of 18.2% and stable power output efficiency of 17.1% during MPP tracking. In this work, it is demonstrated that in the LBG perovskite thin films grown by VAGC, the radiative recombination is dominating compared to the LBG perovskite thin films grown by the antisolvent method. Furthermore, the VAGC demonstrate high reproducibility and good performance in LBG PSCs with active areas of up to 1 cm^2. Making use of the LBG PSC ($E_G \approx 1.27$ eV) developed in this work, a 4T all-perovskite tandem solar cell with a reverse J–V PCE as high as 23% is demonstrated.

Experimental Section

Preparation of the Precursor Solution for the LBG $FA_{0.8}MA_{0.2}Sn_{0.5}Pb_{0.5}I_3$ Absorber: The optimized LBG (LBG) perovskite solution was prepared by mixing 0.7 M tin iodide (SnI$_2$, Alfa Aesar, 99.999%), 0.7 M lead iodide (PbI$_2$, 99.9985%), 0.008 M lead thiocyanate (Pb(SCN)$_2$, Sigma Aldrich, 99.5%), 0.048 M tin fluoride (SnF$_2$, Sigma Aldrich, 99%), 1.15 M formamidinium iodide (FAI, GreatCell Solar), and 0.29 M methylammonium iodide (MAI, GreatCell Solar) in the 9:1 (volume ratio) mixture of *N,N*-dimethylformamide (DMF, Sigma Aldrich, anhydrous, 99.8%) and dimethyl sulfoxide (DMSO, Sigma Aldrich, anhydrous, ≥99.9%). The solution was kept at room temperature for three hours to ensure that all precursor materials were dissolved. The perovskite solution was prepared with a 1:1 stoichiometric molar ratio of Sn and Pb as well as a 4:1 stoichiometric molar ratio of FA and MA. The final perovskite composition is estimated to be FA$_{0.8}$MA$_{0.2}$Sn$_{0.5}$Pb$_{0.5}$I$_3$. The perovskite solution was prepared in a N$_2$ glovebox (O$_2$ < 0.2 ppm, and H$_2$O < 0.4 ppm). The solution was processed immediately after preparation.

Preparation of the Precursor Solution for the WBG $Cs_{0.1}(MA_{0.17}FA_{0.83})_{0.9}Pb(I_{0.83}Br_{0.17})_3$ Absorber: The precursor solution was prepared by mixing methylammonium bromide (MABr), formamidinium iodide (FAI), lead iodide (PbI$_2$), and lead bromide (PbBr$_2$) in 4:1 DMF and DMSO with molar ratios of 0.2, 1, 1.1, and 0.2 M, respectively. A CsI stock solution (1.5 M in DMSO) was then added to form a Cs$_{0.1}$(MA$_{0.17}$FA$_{0.83}$)$_{0.9}$Pb(I$_{0.83}$Br$_{0.17}$)$_3$ perovskite stoichiometry.

Deposition of the WBG $Cs_{0.1}(MA_{0.17}FA_{0.83})_{0.9}Pb(I_{0.83}Br_{0.17})_3$ Absorber: For the deposition of the thin films, the as-prepared solution was spin-coated in two steps: 1) 1000 rpm for 10 s and 2) 6000 rpm for 20 s. 7 s before the end of the spin coating, 100 µL of chlorobenzene was dripped as antisolvent on the wet film. The samples were then annealed at 100 °C for 1 h. Deposition and annealing of the perovskite absorber were conducted in a nitrogen-filled glovebox (O$_2$ < 0.2 ppm, and H$_2$O < 0.4 ppm).

Deposition of the LBG $FA_{0.8}MA_{0.2}Sn_{0.5}Pb_{0.5}I_3$ Absorber by the Antisolvent Method: For the LBG perovskite thin films prepared by the antisolvent method, the perovskite solution was spin-coated on a PEDOT:PSS-coated substrate at 6000 rpm for 50 s. 150 µL of chlorobenzene was dripped on the wet film 12 s after the start of the spin coating. Subsequently, the substrates were annealed at 100 °C for 6 min.

Deposition of the LBG $FA_{0.8}MA_{0.2}Sn_{0.5}Pb_{0.5}I_3$ Absorber by the Vacuum-Assisted Growth Control (VAGC) Method: Deposition of the LBG perovskite thin films by VAGC was conducted by spin-coating the perovskite solution on the PEDOT:PSS substrate at 5000 rpm for 12 s. The still wet films were then directly transferred into a vacuum chamber (≈10 Pa) with a 150 mL volume size. After different times of vacuum exposure (2, 5, 10, and 30 s), the perovskite thin films were annealed at 100 °C for 6 min. The perovskite thin films exhibit a thickness of ≈600 nm. Deposition, vacuum treatment, and annealing of the perovskite thin films were conducted in a nitrogen-filled glovebox (O$_2$ < 0.2 ppm, and H$_2$O < 0.4 ppm). See the supporting videos and description in the Supporting Information.

Fabrication of the LBG Perovskite Solar Cells: The LBG solar cells were fabricated in planar device architecture based on the thin films stack sequence glass/indium tin oxide (ITO)/PEDOT:PSS/FA$_{0.8}$MA$_{0.2}$Sn$_{0.5}$Pb$_{0.5}$I$_3$/PCBM/C60/BCP/Ag. The glass substrates were coated with a 140 nm thick ITO thin film (sheet resistance 15 Ω sq^{-1}, Luminescence Technology). These substrates were cleaned consecutively in deionized (DI) water, acetone, and isopropanol in an ultrasonic bath for 10 min each. Right before the deposition of the hole transport layer, the substrates are treated in an oxygen plasma for 3 min. A thin (≈25 nm) poly(3,4-ethylenedioxythiophene) polystyrene sulfonate (PEDOT:PSS, Ossila, AI 4083) hole transport layer was deposited (as received) on the cleaned ITO substrate by spin coating (4000 rpm for 50 s), followed by annealing at 175 °C for 30 min. After the deposition of the perovskite thin film using the VAGC or antisolvent method, a thin film (≈5 nm) of 6,6-phenyl C$_{61}$ butyric acid methyl ester (PCBM, Sigma Aldrich, 99.5%) was deposited on the perovskite thin film using a 5 mg mL^{-1} solution in 1,2-dichlorobenzene (Sigma Aldrich, anhydrous, 99%). Afterward, two thin films of the fullerene (C$_{60}$, ≈20 nm) and 2,9-dimethyl-4,7-diphenyl-1,10-phenanthroline (BCP, ≈5 nm) were thermally evaporated as the electron transport material, followed by the deposition of a Ag rear electrode (≈100 nm). The active area of the solar cells was 0.105 cm^{-2} or 1 cm^2.

Fabrication of Semitransparent WBG Solar Cells: The semitransparent WBG solar cells were fabricated in planar device architecture based on the thin-film stack sequence glass/ITO/SnO$_2$/perovskite/spiro-MeOTAD/MoO$_3$/ITO/MgF$_2$. SnO$_2$ nanoparticles (Alfa Aesar, diluted by deionized water to 2% volume ratio) were spin-coated at a speed of 4000 rpm for 30 s on the ITO substrate, followed by an annealing step at 250 °C for 30 min in air. As hole transport layer, a spiro-MeOTAD thin film was deposited on the absorber. For that, 80 mg spiro-MeOTAD was dissolved in 1 ml of chlorobenzene and doped with 17.5 µL of a lithium salt solution (520 mg mL^{-1} of lithium bis(trifluoromethanesulfonyl) imide in acetonitrile) and 28.5 µL of 4-tetra-butylpyridine. The solution was spin-coated on the absorber at 4000 rpm for 30 s inside the glovebox. A 15 nm thick MoO$_x$ buffer thin film was deposited on top of spiro-MeOTAD by thermal evaporation before the deposition of the rear electrode. For the fabrication of the rear electrode, ITO (200 nm) was sputtered on the device by using a Lesker sputtering system. The deposition was carried out at room temperature (25 °C) at a process pressure of 0.8 mTorr. The process gas was argon with 2.5% oxygen pressure. The conductivity of the ITO was further improved by evaporation of gold fingers (60 nm) on top of the ITO. A 200 nm thick MgF$_2$ thin film was thermally evaporated on the ITO in order to improve the transmission into the sub solar cell.

Sample Characterization—Current-Density–Voltage (J–V) Measurements: The J–V characteristics of the LBG and semitransparent WBG PSCs were measured with a class AAA solar simulator (Newport Oriel Sol3A) at a power density of 100 mW cm^{-2}, simulating AM 1.5G solar irradiation. The scan rate during measurement was set to 0.6 V s^{-1} using a sourcemeter (Keithley 2400A). The solar simulator was calibrated with a certified Si solar cell (Newport) equipped with a KG5 band pass filter. The stable power output efficiency of the PSCs was determined by tracking the maximum power point (MPP) under continuous AM 1.5G illumination. The temperature of the devices was actively controlled by a Peltier element connected to a microcontroller and set to 25 °C while conducting the J–V analyses and

**ADVANCED
SCIENCE NEWS**

www.advancedsciencenews.com

**ADVANCED
ENERGY
MATERIALS**

www.advenergymat.de

MPP tracking. For measuring the photovoltaic characteristics of 4T-all PSC, the bottom LBG PSC was placed underneath a semitransparent WBG PSC.

Sample Characterization—Scanning Electron Microscopy (SEM): Field emission cross-sectional and top-view scanning electron microscopy (SEM) images of LBG perovskite were taken with a ZEISS Supra60 VP scanning electron microscope.

Kelvin-Probe Force Microscopy (KPFM) Measurement: The KPFM analyses was conducted stand-alone atomic force microscope (Asylum Research MFP-3D) with a conductive silicon cantilever coated with platinum (HQ: NSC18/Pt). The measurements of the topography and the contact potential difference (CPD) was performed in 28 nm over the sample surface in the air. For line profiles, an average of 5 pixels was chosen and the line position was at the middle of the taken images.

Optical Characterization and External Quantum Efficiency (EQE) Measurements: The absorption spectra of the perovskite thin films and devices were measured with a Bentham PVE300 photovoltaic service characterization system by illuminating the solar cell with modulated monochromatic light.

X-Ray Diffraction (XRD): The crystal structure of the perovskite thin films was examined by X-ray diffraction (Bruker D2Phaser) with Cu Kα radiation (λ = 1.5405 Å) in Bragg–Brentano configuration using a LynxEye detector. The X-ray data were taken from unfinished devices on glass/ITO/PEDOT:PSS substrates.

Steady-State and Time-Resolved Photoluminescence (PL) Spectroscopy: Transient PL measurements were performed using a streak camera system (Hamamatsu Universal Streak Camera C10910) coupled to a spectrometer (Acton SpectraPro SP2300). The streak camera was used in single sweep mode to allow for a 1000 ns time window and a full width at half maximum (FWHM) of the instrumental response function of 20 ns. For the excitation, a mode-locked Ti:sapphire laser (Coherent, Chameleon Ultra) with a pulse width of 140 fs and a repetition rate of 80 MHz was used. The light output was frequency doubled by a second harmonic generator (Coherent, Chameleon Compact OPO-Vis) and the repetition rate reduced to 0.7 MHz using a pulse picker (APE pulseSelect). All transient PL spectra were measured with a wavelength of 530 nm and a pump fluence of 46 nJ cm^{-2}. For the PL measurement of the Perovskite with and without PCBM/C60 on glass substrate, the glass-glass encapsulation was used, as PMMA solution can wash away the PCBM and C60.

X-Ray Photoelectron Spectroscopy (XPS) Measurements: For XPS, LBG absorbers prepared via the VAGC and the antisolvent method were sealed under inert atmosphere and introduced into the ultrahigh vacuum (UHV) system without air exposure.[42] The XPS measurements were performed in the materials for energy (MFE) laboratory at KIT with an Omicron Argus CU electron analyzer and a non-monochromatized DAR 450 twin anode X-ray source providing Mg K$_\alpha$ and Al K$_\alpha$ X-rays. The energy axis was calibrated using a sputter-cleaned Au, Ag, and Cu foil.[43] To prevent an influence of beam-induced changes from the X-rays on the spectra, measurement times were kept <10 min. This upper limit of the measurement time was determined in time-resolved measurements in the course of this study.

Supporting Information

Supporting Information is available from the Wiley Online Library or from the author.

Acknowledgements

Conflict of Interest

The authors declare no conflict of interest.

Keywords

[1] M. R. Filip, G. E. Eperon, H. J. Snaith, F. Giustino, *Nat. Commun.* **2014**, *5*, 5757.

[2] Y.-M. You, W.-Q. Liao, D. Zhao, H.-Y. Ye, Y. Zhang, Q. Zhou, X. Niu, J. Wang, P.-F. Li, D.-W. Fu, Z. Wang, S. Gao, K. Yang, J.-M. Liu, J. Li, Y. Yan, R.-G. Xiong, *Science* **2017**, *357*, 306.

[3] W.-Q. Liao, D. Zhao, Y.-Y. Tang, Y. Zhang, P.-F. Li, P.-P. Shi, X.-G. Chen, Y.-M. You, R.-G. Xiong, *Science* **2019**, *363*, 1206.

[4] Best Research-Cell Efficiencies, National Renewable Energy Laboratory, https://www.nrel.gov/pv/cell-efficiency.html (accessed: June 2019).

[5] S. Gharibzadeh, B. Abdollahi Nejand, M. Jakoby, T. Abzieher, D. Hauschild, S. Moghadamzadeh, J. A. Schwenzer, P. Brenner, R. Schmager, A. A. Haghighirad, L. Weinhardt, U. Lemmer, B. S. Richards, I. A. Howard, U. W. Paetzold, *Adv. Energy Mater.* **2019**, *9*, 1803699.

[6] F. Sahli, J. Werner, B. A. Kamino, M. Bräuninger, R. Monnard, B. Paviet-Salomon, L. Barraud, L. Ding, J. J. Diaz Leon, D. Sacchetto, G. Cattaneo, M. Despeisse, M. Boccard, S. Nicolay, Q. Jeangros, B. Niesen, C. Ballif, *Nat. Mater.* **2018**, *17*, 820.

[7] H. Shen, T. Duong, J. Peng, D. Jacobs, N. Wu, J. Gong, Y. Wu, S. K. Karuturi, X. Fu, K. Weber, X. Xiao, T. P. White, K. Catchpole, *Energy Environ. Sci.* **2018**, *11*, 394.

[8] D. Zhao, K. Zhu, K. Yu, C. Chen, X. Zhao, Z. Song, C. Wang, Y. Yan, *ACS Energy Lett.* **2018**, *3*, 305.

[9] D. Zhao, C. Chen, C. Wang, M. M. Junda, Z. Song, C. R. Grice, Y. Yu, C. Li, B. Subedi, N. J. Podraza, X. Zhao, G. Fang, R. G. Xiong, K. Zhu, Y. Yan, *Nat. Energy* **2018**, *3*, 1093.

[10] G. E. Eperon, T. Leijtens, K. A. Bush, R. Prasanna, T. Green, J. T.-W. Wang, D. P. McMeekin, G. Volonakis, R. L. Milot, R. May, A. Palmstrom, D. J. Slotcavage, R. A. Belisle, J. B. Patel, E. S. Parrott, R. J. Sutton, W. Ma, F. Moghadam, B. Conings, A. Babayigit, H.-G. Boyen, S. Bent, F. Giustino, L. M. Herz, M. B. Johnston, M. D. McGehee, H. J. Snaith, *Science* **2016**, *354*, 861.

[11] https://www.pv-tech.org/news/.

[12] J. Tong, Z. Song, D. H. Kim, X. Chen, C. Chen, A. F. Palmstrom, P. F. Ndione, M. O. Reese, S. P. Dunfield, O. G. Reid, J. Liu, F. Zhang, S. P. Harvey, Z. Li, S. T. Christensen, G. Teeter, D. Zhao, M. M. Al-Jassim, M. F. A. M. van Hest, M. C. Beard, S. E. Shaheen, J. J. Berry, Y. Yan, K. Zhu, *Science* **2019**, *7911*, 7911.

[13] D. A. Ritchie, H. Glass, A. Sadhanala, R. H. Friend, W. Nie, M. Tabachnyk, B. Zhao, A. J. Pearson, A. D. Mohite, K. C. Gödel, Y. Puttisong, S. E. Dutton, H. E. Beere, M. Abdi-Jalebi, V. S. Kamboj, *Adv. Mater.* **2016**, *29*, 1604744.

[14] G. Kapil, T. S. Ripolles, K. Hamada, Y. Ogomi, T. Bessho, T. Kinoshita, J. Chantana, K. Yoshino, Q. Shen, T. Toyoda, T. Minemoto, T. N. Murakami, H. Segawa, S. Hayase, *Nano Lett.* **2018**, *18*, 3600.

[15] D. Zhao, Y. Yu, C. Wang, W. Liao, N. Shrestha, C. R. Grice, A. J. Cimaroli, L. Guan, R. J. Ellingson, K. Zhu, X. Zhao, R.-G. Xiong, Y. Yan, *Nat. Energy* **2017**, *2*, 17018.

[16] K. Zhu, N. Shrestha, C. Wang, N. J. Podraza, Y. Xiao, C. R. Grice, D. Zhao, Y. Yu, A. J. Cimaroli, W. Liao, Y. Yan, K. Ghimire, R. J. Ellingson, R.-G. Xiong, *J. Am. Chem. Soc.* **2016**, *138*, 12360.

[17] R. Prasanna, A. Gold-Parker, T. Leijtens, B. Conings, A. Babayigit, H. G. Boyen, M. F. Toney, M. D. McGehee, *J. Am. Chem. Soc.* **2017**, *139*, 11117.

[18] Q. Li, Y. Pan, J. Guo, Y. Chen, H. Zhang, W. Huang, Y. Xia, Z. Shi, *Adv. Mater.* **2017**, *29*, 1605005.

[19] T. Leijtens, R. Prasanna, K. A. Bush, G. E. Eperon, J. A. Raiford, A. Gold-Parker, E. J. Wolf, S. A. Swifter, C. C. Boyd, H. P. Wang, M. F. Toney, S. F. Bent, M. D. McGehee, *Sustainable Energy Fuels* **2018**, *2*, 2450.

[20] C. M. Tsai, H. P. Wu, S. T. Chang, C. F. Huang, C. H. Wang, S. Narra, Y. W. Yang, C. L. Wang, C. H. Hung, E. W. G. Diau, *ACS Energy Lett.* **2016**, *1*, 1086.

[21] K. P. Marshall, M. Walker, R. I. Walton, R. A. Hatton, *Nat. Energy* **2016**, *1*, 16178.

[22] W. Liao, D. Zhao, Y. Yu, C. R. Grice, C. Wang, A. J. Cimaroli, P. Schulz, W. Meng, K. Zhu, R. G. Xiong, Y. Yan, *Adv. Mater.* **2016**, *28*, 9333.

[23] T. Handa, R. Nishikubo, Y. Murata, Y. Hashikawa, Y. Katsuki, Y. Shimakawa, J. Liu, A. Saeki, A. Wakamiya, T. Saito, Y. Kanemitsu, S. Yakumaru, M. Ozaki, *ACS Omega* **2017**, *2*, 7016.

[24] Z. Yang, A. Rajagopal, A. K. Y. Jen, *Adv. Mater.* **2017**, *29*, 1704418.

[25] H. Zhang, H. L. Zhu, Y. Zhao, J. Mao, W. C. H. Choy, J. Xiao, *Adv. Funct. Mater.* **2017**, *27*, 1605469.

[26] Q. Jiang, Z. Chu, P. Wang, X. Yang, H. Liu, Y. Wang, Z. Yin, J. Wu, X. Zhang, J. You, *Adv. Mater.* **2017**, *29*, 1703852.

[27] H. Rao, W. Sun, S. Ye, Z. Liu, Y. Li, C. Huang, W. Yan, Z. Bian, H. Zhou, Z. Zhao, H. Peng, *Adv. Energy Mater.* **2016**, *6*, 1601353.

[28] C. Li, Z. Song, D. Zhao, C. Xiao, B. Subedi, N. Shrestha, M. M. Junda, C. Wang, C. S. Jiang, M. Al-Jassim, R. J. Ellingson, N. J. Podraza, K. Zhu, Y. Yan, *Adv. Energy Mater.* **2019**, *9*, 1803135.

[29] W. Qiu, T. Merckx, M. Jaysankar, C. Masse De La Huerta, L. Rakocevic, W. Zhang, U. W. Paetzold, R. Gehlhaar, L. Froyen, J. Poortmans, D. Cheyns, H. J. Snaith, P. Heremans, *Energy Environ. Sci.* **2016**, *9*, 484.

[30] Y. Wang, W. Fu, J. Yan, J. Chen, W. Yang, H. Chen, *J. Mater. Chem. A* **2018**, *6*, 13090.

[31] D. Zhao, C. Chen, C. Wang, M. M. Junda, Z. Song, C. R. Grice, Y. Yu, C. Li, B. Subedi, N. J. Podraza, X. Zhao, G. Fang, R.-G. Xiong, K. Zhu, Y. Yan, *Nat. Energy* **2018**, *3*, 1093.

[32] S. Paek, P. Schouwink, E. N. Athanasopoulou, K. T. Cho, G. Grancini, Y. Lee, Y. Zhang, F. Stellacci, M. K. Nazeeruddin, P. Gao, *Chem. Mater.* **2017**, *29*, 3490.

[33] X. Li, D. Bi, C. Yi, J.-D. Décoppet, J. Luo, S. M. Zakeeruddin, A. Hagfeldt, M. Grätzel, *Science* **2016**, *353*, 58.

[34] K. H. Hendriks, J. J. Van Franeker, B. J. Bruijnaers, J. A. Anta, M. M. Wienk, R. A. J. Janssen, *J. Mater. Chem. A* **2017**, *5*, 2346.

[35] T. Abzieher, S. Moghadamzadeh, F. Schackmar, H. Eggers, F. Sutterlüti, A. Farooq, D. Kojda, K. Habicht, R. Schmager, A. Mertens, R. Azmi, L. Klohr, J. A. Schwenzer, M. Hetterich, U. Lemmer, B. S. Richards, M. Powalla, U. W. Paetzold, *Adv. Energy Mater.* **2019**, *9*, 1802995.

[36] R. Wang, M. Zhuo, J. Li, T. Zhai, J. Yang, K. Fu, L. Liao, L. Liu, S. Duhm, *Adv. Mater.* **2019**, *6*, 1801827.

[37] S. Prathapani, D. Choudhary, S. Mallick, P. Bhargava, A. Yella, *CrystEngComm* **2017**, *19*, 3834.

[38] A. Sadhanala, F. Deschler, T. H. Thomas, S. E. Dutton, K. C. Goedel, F. C. Hanusch, M. L. Lai, U. Steiner, T. Bein, P. Docampo, D. Cahen, R. H. Friend, *J. Phys. Chem. Lett.* **2014**, *5*, 2501.

[39] D. Zhao, C. Zhang, H. Kim, L. J. Guo, *Adv. Energy Mater.* **2015**, *5*, 2.

[40] K. A. Bush, A. F. Palmstrom, Z. J. Yu, M. Boccard, R. Cheacharoen, J. P. Mailoa, D. P. McMeekin, R. L. Z. Hoye, C. D. Bailie, T. Leijtens, I. M. Peters, M. C. Minichetti, N. Rolston, R. Prasanna, S. Sofia, D. Harwood, W. Ma, F. Moghadam, H. J. Snaith, T. Buonassisi, Z. C. Holman, S. F. Bent, M. D. McGehee, *Nat. Energy* **2017**, *2*, 17009.

[41] Q. Han, Y.-T. Hsieh, L. Meng, J.-L. Wu, P. Sun, E.-P. Yao, S.-Y. Chang, S.-H. Bae, T. Kato, V. Bermudez, Y. Yang, *Science* **2018**, *361*, 904.

[42] L. Weinhardt, D. Hauschild, C. Heske, *Adv. Mater.* **2019**, *31*, 1806660.

[43] C. D. Wagner, G. E. Muilenberg, *Handbook of X-Ray Photoelectron Spectroscopy*, Perkin-Elmer, Eden Prairie, MN **1979**.